instruments

MDPI

Article

Practical Aspects of Multiwavelength Analytical Ultracentrifugation

Joseph Pearson and Helmut Cölfen *

Physical Chemistry, University of Konstanz, 78457 Konstanz, Germany; joe.pearson@uni-konstanz.de
* Correspondence: helmut.coelfen@uni-konstanz.de; Tel.: +49-7531-88-4063

Received: 18 February 2019; Accepted: 15 March 2019; Published: 21 March 2019

Abstract: Open-source Multiwavelength Analytical Ultracentrifugation (MWL-AUC) detection systems have been evolving for over a decade. Continual advances emerging out of several research groups have brought the instrumentation technology to increasingly higher levels of performance. The capabilities of MWL-AUC have been documented in many publications, demonstrating the applicability of broad spectrum absorbance acquisitions in analytical ultracentrifugation to a wide array of scientific fields. Despite numerous examples of the usefulness and unique advantages of MWL-AUC, the adoption of the technology by more research groups has been slow. The complexity of the hardware, integration within an ultracentrifuge platform and lack of practical construction and operational information is the likely source of reluctance. Here, we clearly describe the challenges facing a researcher considering adopting MWL-AUC technology in their own laboratories, and provide the information necessary to implement and operate a MWL-AUC system. The discussion includes details of detector assembly, optical alignment, and acquisition parameter settings necessary to achieve high quality experimental results.

Keywords: analytical ultracentrifugation; multiwavelength; Open-AUC

1. Introduction

Past publications on MWL-AUC have described the overarching principles, demonstrated the technical achievements and illustrated the potential uses of this technology. Many of the basic concepts and original design schemes for the hardware have been reported previously [1–5]. This manuscript provides additional details that have not yet been described or were more recently adapted, but have proven essential to producing high quality measurements from the instrument. We hope to present a realistic portrayal of the challenges a researcher faces when considering implementing one of these systems in their own laboratory, in addition to many of the critical aspects of the installation that we have found necessary for successful instrument operation demonstrated in past publications [2,6–8]. This includes a description of the necessary tools and expertise to build and install the detector, followed by a protocol for alignment and calibration. Finally, we discuss setting the operating parameters and considerations of experimental design for various types of sample investigations. Early design iterations of the open-source MWL-AUC hardware featured lens-based illumination and imaging optics. The integration of mirror-based illumination and imaging optics, free of chromatic aberration, has been described recently and is the subject of the alignment and focusing protocol in the following discussion [2,9]. In addition to the open-source MWL-AUC mirror optics hardware detailed here, a commercial spin-off version of the detector has been introduced by Nanolytics© of Potsdam [10].

2. Materials and Methods

A MWL detector, which was built according to the Open AUC project standards, is composed of an illumination source, optical scanning assembly and spectrometer, retrofitted into a Beckman Coulter ultracentrifuge platform [11]. Many of the components may be ordered as stock items from the respective suppliers, while the aluminum mechanical assembly must be custom fabricated by a machine shop. An up to date parts list for all of the stock items, and schematics of the custom aluminum hardware, is available upon request from the authors or can be downloaded from http://wiki.aucsolutions.com/openAUC/. This includes the Beckman Coulter ultracentrifuge and hardware to build the detector. In addition, a Beckman Coulter analytical ultracentrifuge rotor, sample cells, and counterbalance cell will need to be purchased. The control software—MWL–OS—was developed by Johannes Walter, and operates on the latest versions of LabVIEW by National Instruments Corporation, Austin Texas [12]. The MWL–OS interfaces with a National Instruments PCI-6602 Counter/Timer Card for synchronization signal acquisition and generation. Earlier designs capture a rotor timing pulse from the Hall effect sensor that is standard to the centrifuges. Later adaptations use a reflective optical sensor that tracks a reflective strip polished into the bottom of the rotor, and provides a more reliable signal. The electronics schematics for the reflective optical sensor are provided in Appendix A.

3. Installation, Alignment and Calibration of a MWL Detector

3.1. Centrifuge Modifications for Detector Installation

The Optima series preparative XL and XPN series analytical ultracentrifuges from Beckman Coulter have nearly identical heat sink hardware in terms of dimensions, and can both be modified to mount a MWL detector. It is recommended to use a centrifuge with a turbomolecular pump so as to limit oil vapor contamination of the optics [13]. Centrifuge modification requires disassembly of the centrifuge chamber and involves only basic mechanics tools. However, removal of the drive is an awkward procedure, and is best performed by someone competent in mechanics. The following procedure describes the basic procedure and references part numbers identified in Figure 1 through 7. The figures include images of the detection system in a XL-A-modified centrifuge and the construction of a system within an Optima preparative style centrifuge. A complete list of numbered items in the figures is included below. The centrifuge modifications require drilling threaded holes in the bottom of the centrifuge chamber, and cutting a channel through the thermal can (Figure 1a #1) for the MWL scanning assembly. The centrifuge chamber is a thick steel cylinder with sliding lid. A thin aluminum thermal can (Figure 1a #1) sits in the chamber extending up the sides. Eight thermoelectric elements (Figure 1b #2) are sandwiched between the bottom of the thermal can and the bottom of the chamber, providing temperature regulation by thermal radiation while the chamber is under vacuum. The bottom of the chamber, which holds the electric drive, also provides heat transfer for the thermoelectric elements outside the AUC, and is referred to as the heat sink (Figure 1b #3). The thermoelectric modules are coated in thermal paste to provide heat transfer to the thermal can. Heating the thermal can with a heat gun just prior to removal helps to loosen the thermal paste such that the thermal can be removed without damaging the thermoelectric modules beneath. A 2.0 cm-wide channel (Figure 1d #4) may then be cut in the thermal can to allow the bottom of the MWL detector arm to slide freely below the rotor.

Removal of the heat sink requires detaching the electric drive. The drive (Figure 1c #5) is disconnected from the heat sink by recessed nuts (Figure 1c #6) below the can on the upper edge of the drive. A small scissor lift (Figure 1c #7) is useful for supporting and lowering the drive during removal. Care should be taken so that none of the greased rubber gaskets (Figure 1c #8) are damaged or dirtied during this process. Furthermore, it is important to keep the drive in the vertical position shown in Figure 1c because otherwise the drive oil will flow out.

Threaded holes (Figure 1d #9) may then be drilled in the heat sink bottom to accommodate the electrical and fiber optic vacuum feedthroughs. The holes drilled in the bottom of the chamber

are of a similar dimension to those installed by Beckman Coulter for the absorbance or interference optics, and thereby impose no structural difference to the chamber integrity than that of a commercial AUC. However, the Beckman warranty will be lost upon the described modifications of the heat sink. Alternatively, with a XL-A/XL-I heat sink, the hole for the monochromator may be repurposed for cable feedthroughs, but this still requires an additional custom feedthrough mounting component (Figure 1e #10), as described in early publications on this detector [3]. Assembly of the heat sink, drive and thermal can is the reverse of removal. The use of a XL-A/XL-I heat sink is a useful option for laboratories where drilling holes through the bottom of the chamber are a prohibitive concern. However, the acquisition of an XL-A/XL-I heat sink is more expensive.

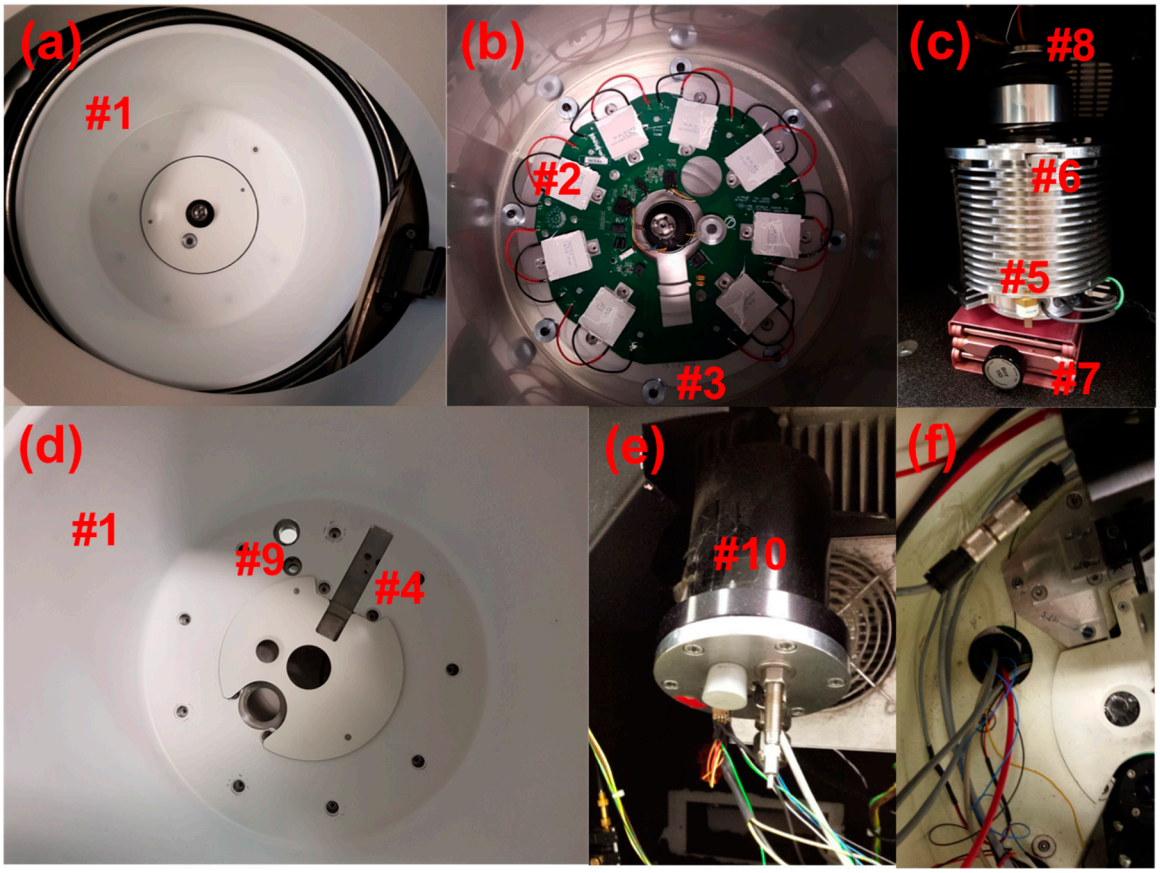

Figure 1. (**a**) Preparative centrifuge chamber; thermal can, chamber lid. (**b**) Preparative centrifuge chamber with the Thermal can removed; thermoelectric elements, heat sink. (**c**) Preparative centrifuge drive; small scissor lift, drive connection nut, drive gasket. (**d**) Preparative centrifuge thermal can with feedthrough holes and slot cut; holes for fiber optic feed through and electrical feedthrough, slot for multiwavelength (MWL) illumination assembly, and extra hole added for installing interferometer optics. (**e**) Custom feedthrough mounting component for repurposing XL-A monochromator hole. (**f**) Wires and fiber optic cables coming through repurposed monochromator hole in XL-A converted open-source multiwavelength analytical ultracentrifugation (MWL-AUC) machine.

Extra threaded holes (Figure 2e #11) may also need to be added to the heat sink for mounting the detector arm (Figure 2f #12), depending on if the heat sink comes from a preparative or analytical centrifuge. The base of the detector arm has been designed with alternative configurations (Figure 3b #13) and (Figure 2h #14) to mount within the respective heat sink. For mounting within the XL-A type heat sink, two separate base plates (Figure 2e #15) are attached by three screws to the heat sink below each side of the detector arm base. Four of the screws use the existing holes (Figure 2e #16) normally used for attaching the thermal can to the heat sink, and two more screws are inserted in new

holes (Figure 2e #11) near the back of the detector arm position to provide a third point of stability. This is a modification that was adapted to the original design, and was found to be necessary for additional stability when leveling the detector arm. When using a preparative centrifuge type heat sink (Figure 1b #3) and corresponding arm base (Figure 2h #14), no extra holes are required. The base plate screws go through cylinder standoffs Figure 2h (#17) fixing the mounting plates to the heat sink at a height slightly above the thermal can. The current design includes two additional mounting plates (Figure 2g #18) on top of the base plates. The additional mounting plates have a sliding guide block (Figure 2e #19) that is helpful with alignment, as described later. The detector arm is fastened to the mounting plates by two screws through the slotted holes of the detector arm base (Figure 3b #20). Another recent design modification features threaded holes added to each corner of the detector arm base to insert leveling adjustment screws (Figure 2f #21). Fine leveling adjustments of the arm have been shown to be crucial for good radial resolution and avoiding optical artifacts from a misaligned illumination beam [2].

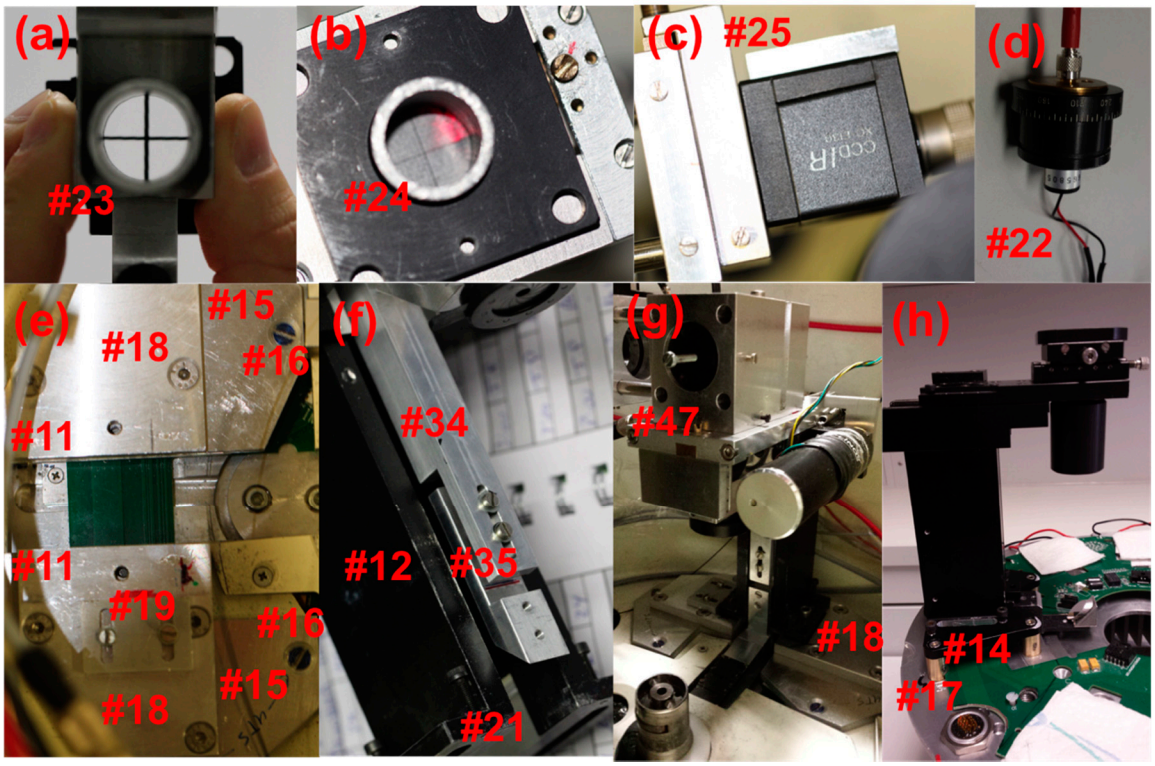

Figure 2. (**a**) Cross-bar device in lower imaging assembly. (**b**) Cross-hair screen mounted above lower imaging assembly; note beam is directed off-center in photo. (**c**) Sony XC-EI30 charge-coupled device (CCD) camera with custom adapter for attaching to the sliding rail assembly. (**d**) SMA fiber optic cable coupled laser diode. (**e**) XL-A type heat sink mounting base plates; holes for mounting to heat sink, additional mounting base plate, sliding guide block, extra arm mounting holes (below additional mounting base plate), cylinder stand offs (below base plate into heat sink). (**f**) Vertical connector: Arm slotted mounting holes with arm leveling screws. (**g**) Open-source MWL arm with mirror optics assembly. (**h**) Nanolytics MWL arm with lens optics assembly.

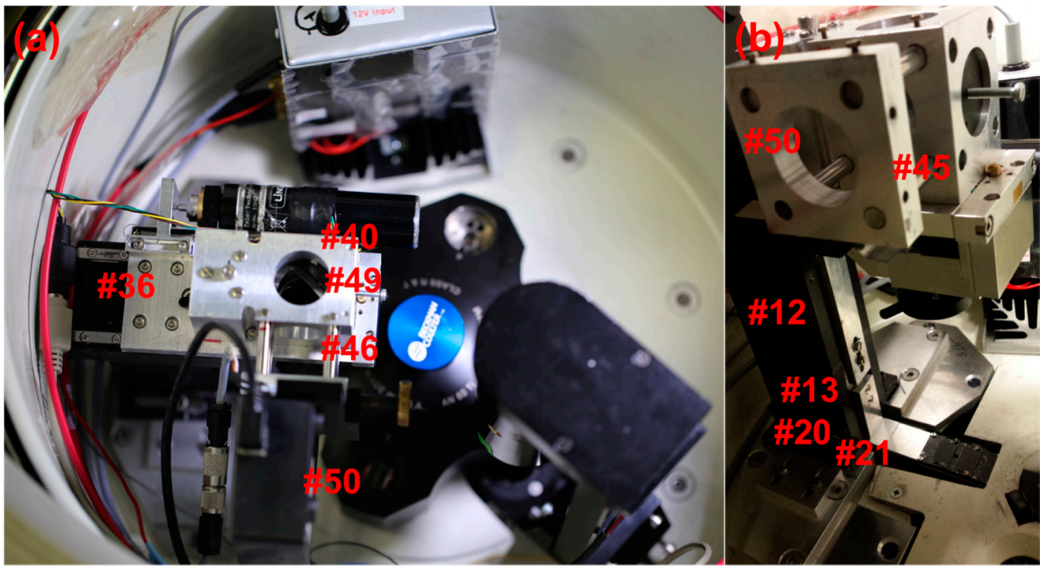

Figure 3. (**a**) Image of the complete MWL detector installed in a preparative centrifuge. An interferometer is also installed in this centrifuge opposite the Arm in addition to an auxiliary electronics box. (**b**) View of the MWL Arm from the side with the spectrometer removed.

3.2. Fundamentals of Detector Installation and Alignment

Installation and alignment of the detector arm must be done simultaneously. A step-by-step protocol for alignment is provided in Appendix B. Here we present an overview of the essential principles of our optics alignment method as they apply to the current detector architecture. However, many of the concepts of the method also apply generally to AUC optical alignment and will be useful for adapting to alternative detector designs.

The installation and alignment of the detector begins at the illumination source and follows the optical path to the detector. A few additional tools are required for the alignment procedure including a small machinists level, SMA adapter-coupled laser diode (Figure 2d #22), a custom cross-bars (Figure 2a #23) and cross-hair screen assembly (Figure 2b #24), and a 2D imaging camera with custom mounting adapter (Figure 2c #25). The laser diode is connected to the input end of the fiber optic cable for the first steps of the optics alignment. A custom slit mask, manufactured by the Universität Konstanz Workshop, covers the output end of the fiber optic cable, inside the chamber, shown in Figure 4c (Figure 4c #26). The slit mask was constructed from two half disks welded onto a 3.2 mm circular plate with a 1 mm center hole. A ~50 µm spacer is held between the two half disks while they are welded to the circular plate. The diameter of the plate is slightly smaller than the diameter of the barrel of an SMA fiber connector tip. A small amount of epoxy at the edge of the slit mask fixes it to the SMA connector tip. Fiber optic cables utilized in this design include adjustable SMA adapters (Figure 4a #27), where the length of the barrel extending from the tip of the connector may be varied. Adjustment of the barrel length is important for collimating the light reflected from the illumination collimating off-axis parabolic mirror (OAPM) (Figure 4a #28). The slit mask covered SMA adapter is inserted into the OAPM, and the SMA barrel length adjusted until good collimation is observed. The laser diode provides a strong beam that may be projected onto a surface 20 to 30 cm away while the room is dark. Good collimation will occur when the tip of the fiber is located precisely at the focal point of the OAPM (Figure 5a #29); 15 mm in this case. It is important to ensure the orientation of the slit mask remains orthogonal to the radial dimension of the mirror in the optical assembly while adjusting for collimation. The beam is slightly distorted due to the slit geometry of the fiber tip opening, this allows for orientation, while still approximating good collimation. Once the beam is collimated it may be installed in the lower illumination assembly (Figure 4a #30), including the illumination focusing OAPM (Figure 4a #31).

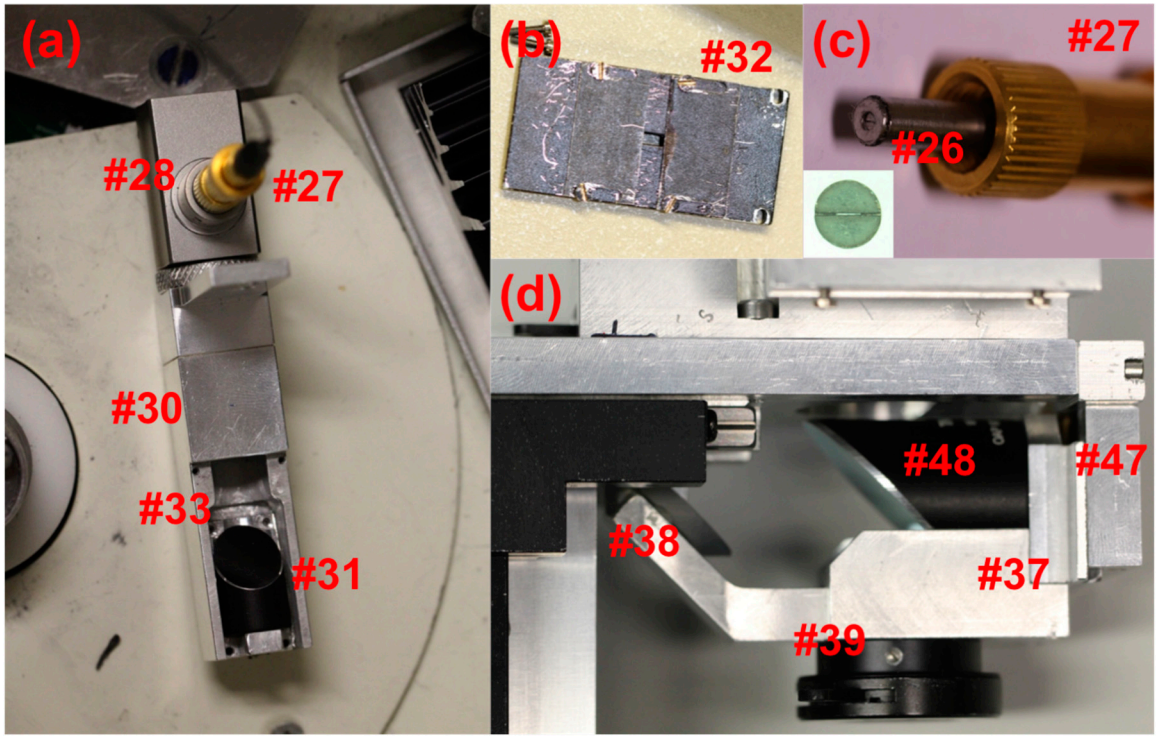

Figure 4. (**a**) Illumination assembly: Adjustable SMA connector, illumination collimating off-axis parabolic mirror (OAPM), illumination focusing OAPM, and focusing OAPM adjustment screws. (**b**) Illumination assembly adjustable aperture. (**c**) Fiber tip slit mask to be mounted on end of SMA connector. Inset showing close up of tip slit mask. (**d**) Lower imaging assembly: lower imaging OAPM, lower iris, and 90° flat mirror.

An adjustable illumination aperture (Figure 4b #32) is positioned over the focusing OAPM on the lower illumination assembly at a later step in the alignment process. With the illumination aperture off, there is access to four adjustment screws (Figure 4a #33) on the focusing OAPM holder. The adjustment screws should be set to the null position prior to installing the lower illumination assembly. The four adjustment screws at each corner of the focusing OAPM holder may be used to adjust the tilt of the mirror and thereby the direction of the illumination beams in a subsequent step. The focusing mirror is also able to slide radially in the illumination assembly channel. The lower illumination assembly is fastened to the sliding stage vertical connector (Figure 4f #34) by two pan head screws after the arm is installed. The sliding stage vertical connector is composed of two pieces, connected by screws through a slot, allowing for vertical adjustment of the lower illumination assembly (Figure 4f #35). This is important for setting the focus plane of the illumination beam, and ensuring the assembly is at a safe distance from the bottom of the rotor. The distance of a Beckman Coulter XL-A optical assembly from the bottom of the rotor in a XL-A centrifuge was measured to be 2.5 mm. This should be considered as a minimum safe working distance, and the lower mirror assembly must be set greater than 2.5 mm from the bottom of the rotor. Fortunately, the focusing OAPM has a focal length of 33 mm, and positioning of the lower assembly such that the beam is focused on the mid plane of the sample channel leaves a space of 3 mm to the bottom of the rotor.

The sliding stage with linear bearings (Figure 3f #36), and vertical connector (Figure 2f #34) should be preinstalled on the detector arm (Figure 3b #12) outside of the chamber. The arm and sliding stage assembly is then installed by carefully lowering it over the fiber optic cable and lower illumination assembly sitting in the channel (Figure 1d #4) of the thermal can, where it will attach to the arm. The arm is fastened to the mounting plates on the heat sink of the rotor by two screws through slotted holes (Figure 3b #20). Screws at the corners of the arm base (Figure 3b #21) allow for

leveling adjustment with the aid of a machinists level. The first installation of the arm requires careful alignment by eye, such that the sliding mechanics of the arm can move along a radial trajectory from the center of the rotor. The arm must also be set such that the sliding range will cover the distance from the top of the sample channel (nearest the rotor center) to the bottom of the channel (nearest the rotor edge). Final testing of the arm alignment is made optically with the aid of a calibration software application, which is part of the LabVIEW© MWL–OS [14]. Once the correct position is determined, it may be fixed for future reference by the positioning of the sliding guide block (Figure 2e #19) along the edge of the arm base. This tool greatly simplifies the alignment procedure and future disassembly of the optics. Once the arm is in place, the lower illumination assembly is fastened to the sliding stage vertical connector by two pan head screws (Figure 2f #34).

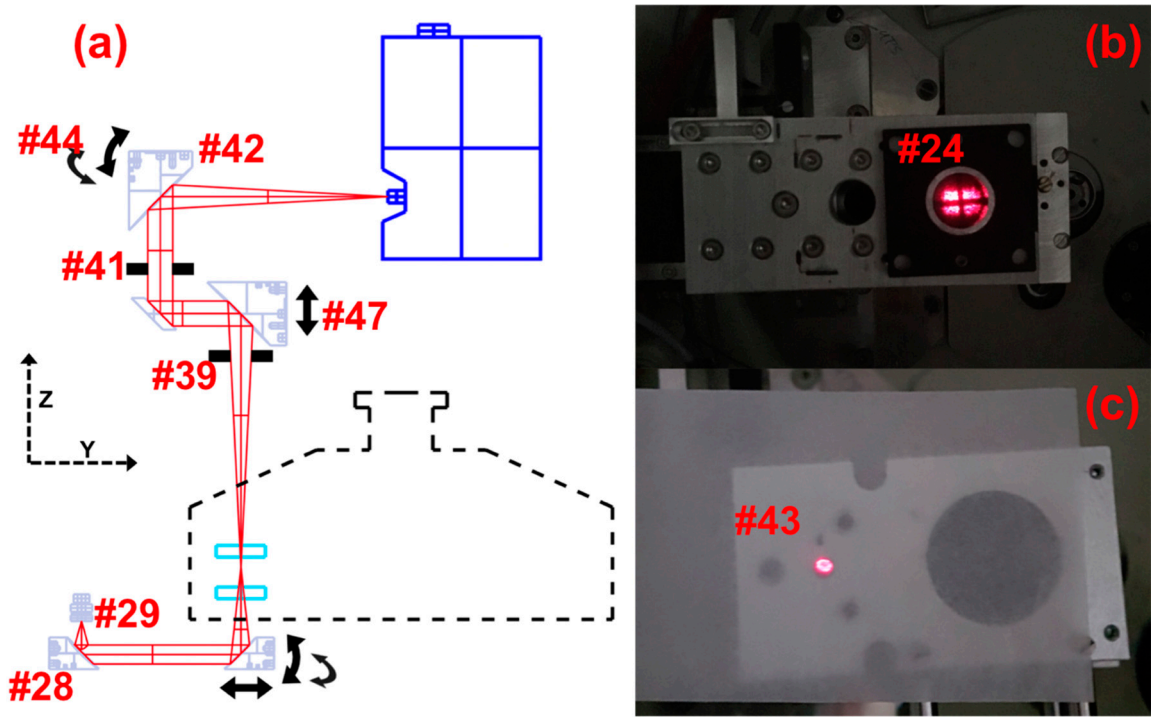

Figure 5. (**a**) Illustration of beam path profile, highlighting the fundamental adjustment points used for illumination and imaging alignment and focusing. (**b**) Image looking down, showing the laser-diode beam and cross-bar shadow projected onto the cross-hair screen. (**c**) Image of second imaging OAPM assembly with OAPM removed, showing the laser diode beam coming through the center hole above the OAPM mounting position. The lower iris is closed to a small hole to provide a narrow beam for centering the second OAPM imaging assembly.

3.3. Beam Collimation and Coincidence

The illumination beam must be aligned parallel and coincident with the optical axis. The alignment relies partially on the precision machining of the mechanical assembly. The focused illumination geometry provides a cone of light. Nevertheless the highest power rays will propagate along the center of the illumination cone and are of primary concern. Custom alignment tools were developed for the following procedure, consisting of a cross-bar (Figure 2a #23) device, and cross-hair screen (Figure 2b #24). The cross-bars device is made up of two 0.7 mm rigid steel bars fixed perpendicular to one another and through the center of a cylindrical adapter that mounts to the first imaging OAPM assembly (Figure 4d #37), directly below the central ray axis of the first imaging OAPM. The first step of beam alignment is performed with the imaging mirrors removed, allowing the illumination beam to pass through the cross-bar cylinder and continue vertically along the central ray axis of the first imaging OAPM position. A second cross-hair cylinder may then be inserted from above,

centered in the same hole as the cylinder holding the cross-bars. The cross-hair cylinder is fitted with a translucent paper screen on top (Figure 5b #24). On the paper screen are printed thin cross-hair lines. The cross-hairs are therefore mechanically centered approximately 10 cm above, and directly over, the cross-bars.

The beam from the laser diode is projected from the illumination optics assembly through the cross-bars cylinder and onto the cross-hair screen where it may be viewed from above (Figure 2b #24). The shadow of the cross-bars is also cast onto the screen. The bright center of the beam, as well as the shadow of the cross-bars, must be centered on the cross-hair screen. Both the beam center and cross-bars shadow may only be centered on the screen when the illumination beam is both parallel and coincident with the optical axis, as illustrated in Figure 6a. Figure 6b–d depicts the possible arrangements of misalignment that should be corrected for by adjustment of the focusing illumination OAPM.

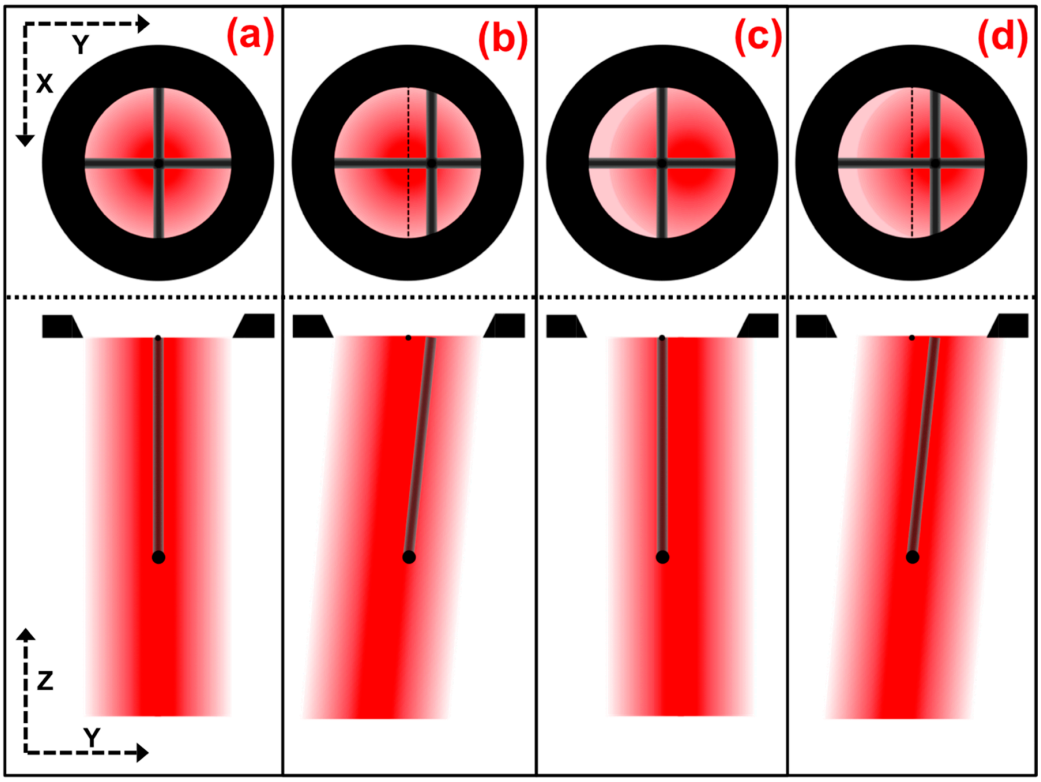

Figure 6. Illustrations of beam alignment: Bottom illustrations are side cross sections of the beam path, showing the beam position and trajectory, and shadow path of the cross bar up to the cross-hair screen opening. Top illustrations are depictions from a view down on the cross-hair screen, showing cross-bar shadow and beam-center alignment for the respective states. (**a**) Illustration of illumination beam alignment parallel and coincident with the optical axis. (**b**–**d**) Illustration of illumination beam in several possible, and commonly occurring, states of misalignment.

Once the illumination beam is aligned, the adjustable illumination aperture (Figure 4b #32) is installed to limit stray light and protect the illumination optics. The aperture plates on top are set approximately 2.5 mm apart, centered over the illumination beam, and are checked by the rectangular beam profile projected onto the screen, see Figure 5b.

3.4. Installation, Alignment, and Focus of the Imaging Optics

The cross-bars and cross-hairs are removed and the first imaging OAPM is installed in the focusing assembly (Figure 4d #37), including the 90° flat mirror (Figure 4d #38) and the lower iris

(Figure 4d #39). The second imaging OAPM assembly (Figure 7a #40) is also installed, including the middle iris (Figure 5a #41), but without the OAPM (Figure 5a #42). When both the irises are closed down to a pinhole, a small beam of light is able to pass through the second imaging OAPM assembly and through the hole centered at the back of the OAPM mounting position. A translucent screen placed over the hole allows for visualization of the beam path, and thereby adjustment of the second imaging OAPM assembly to center (Figure 5c #43). With the second imaging OAPM assembly center fixed, the position is marked, the OAPM is then reinstalled, and the assembly set back to the marked position. The second imaging OAPM is then adjusted to direct the trajectory of the beam projected off the mirror. A Sony XC-EI30 CCD video camera (Figure 2c #25), without lenses and connected to a computer monitor, is used to set the beam direction along the optical axis. The CCD camera is attached to a custom adapter and fitted to the sliding rail assembly (Figure 7a #45), positioning it centered along the optical axis. The sliding rail assembly allows the focusing distance to the camera chip to be adjusted. The imaging OAPMs have a 101.6 mm focal length, therefore the camera is fixed along the sliding rail assembly at 101.6 mm from the center of the second imaging OAPM to plane of the CCD chip.

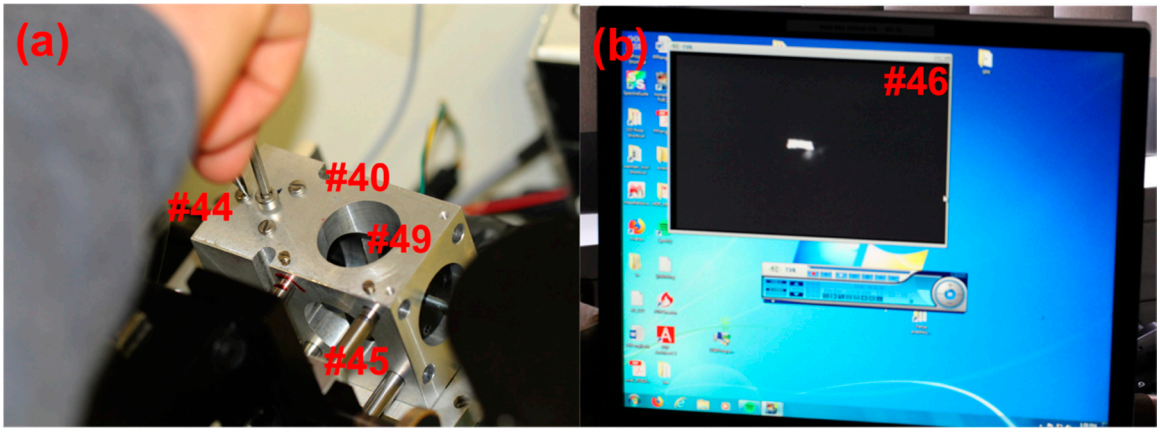

Figure 7. (**a**) Adjustments of the second imaging OAPM made by simultaneously tightening the center screw and loosening one of the three outer screws. In this way, the beam trajectory may be aligned onto the detection window. (**b**) The Sony XC-EI30 CCD video camera shows the image of the illumination slit. Beam alignment by adjusting the second imaging OAPM screws while viewing the slit image position through the CCD video capture.

A low-power light source, such as a pocket flashlight directed at the entrance to the fiber optic cable, is used for the proceeding steps, and must be adjusted so as not to over saturate the CCD chip. The beam direction from the second imaging OAPM is adjusted via the screws (Figure 5a #44) accessible from the top of the second imaging OAPM assembly, and should be carefully moved until the image of the source slit is set at the center of the CCD chip, as viewed on a computer monitor (Figure 7b #46). The first imaging OAPM assembly is then set to focus by the adjustment screw setting (Figure 2g #47) of the first imaging OAPM assembly. The mirror assembly is raised and lowered until the image of the source slit is brought into sharp focus (Figure 7b #46). Note that the first imaging assembly holds the OAPM (Figure 4d #48) and the plane mirror (Figure 4d #38), so the adjustment screw moves both mirrors in unison. When the preceding alignment steps are properly made, adjustment of the lower imaging OAPM assembly will not alter the beam trajectory and the image of the slit will remain centered in the video capture screen, but can be brought in and out of focus. An empty sample cell in the rotor may be introduced in the light path to check the effect of cell windows on mirror focus position, and adjusted as necessary.

In the original design, the spectrometer position extends across the chamber and collides with the interferometer optics also installed on the machine in our lab. A design feature of the assembly

allows the possibly of introducing a second 90° flat mirror (Figure 7a #49), after the second imaging OAPM, positioning the spectrometer mount to the side (Figure 3a #50). The second 90° flat mirror and CCD camera are installed in this arrangement, and then adjusted for alignment and focus. Keep in mind that the first imaging OAPM assembly was set to focus in the preceding steps, and thus the focus position of the spectrometer mount may be determined by again imaging the source slit, without adjustment of the first imaging OAPM. The final step is installation of the spectrometer (Figure 3a #50) and connection of the Xenon flash lamp to the fiber optic cable. With the spectrometer fixed in position, small adjustments of the second imaging OAPM can be made to perfectly center the beam direction onto the spectrometer slit. This will only require movement in the vertical plane of the spectrometer slit position, and can be monitored by intensity readings from the spectrometer. The adjustable iris below the first imaging OAPM (Figure 5a #39) and between OAPMs (Figure 5a #41) allows for setting of the numerical aperture of the optics and limiting stray light. Setting the iris opening to slightly before an intensity drop is observed has been found to yield good results in practice. Further detail on the effects of numerical aperture and optical imaging systems are discussed in Pearson et al. [9].

3.5. Alignment Test and Calibrations

It is absolutely imperative that all mechanical components are tightly fastened, and the sliding stage system is free to move without collision before proceeding to start the rotor. The importance of this step cannot be overstated, and is true for all ultracentrifuge devices. The inertial energy of a spinning titanium rotor is very high and an incident at speed would be catastrophic. To this point, it is also important to set the stepper motor limits so as not to exceed the range of the sliding stage. If the stepper motor were to attempt to extend beyond the limit of the sliding stage it could mechanically fail and fall onto the rotor below. A limit setting must be correctly fixed in the MWL–OS software prior to starting calibrations. The Zaber control software supplied with the motor may be used to manually adjust the position of the motor and note when the sliding stage is near the mechanical limit.

The first calibration step is to ensure the sliding stage scanning vector is aligned with the radial vector of the rotor. The 'Angle Calibration' application in the MWL–OS software plots the rotational angle of flash pulses across a defined interval, and is also used to determine alignment. An angular scan, at 3 krpm, of an empty sample cell is taken at radial positions near the top (nearest to rotor center) and bottom (nearest to the rotor edge) of the cell. The angular position of the sample and reference sector positions are mapped. The difference between the top and bottom angles should be less than 0.25°. If a greater difference is found, the detector arm must be rotated and the procedure repeated until satisfactory. The sliding guide block (Figure 2e #19) greatly simplifies this procedure, as the adjustments required are typically very small. The arm should be releveled after each arm adjustment.

The 'Angular Calibration' application is executed to determine the synchronization timing of the flash lamp for all possible rotor speeds. The cell sector angular position is selected for scans at incremental rotor speed settings in the calibration routine, and the results are fitted to a linear function internally in the software, which may then be used during AUC experiments.

The 'Radial Calibration' application is subsequently executed by scanning the radial dimension of a counterbalance while the rotor is at low speed; 2000 rpm. The edges of the counterbalance mask, on the reference sector side, are set by the manufacturer to be 5.85 mm and 7.15 mm while in the rotor, and serve as reference points from which a radial calibration conversion of the stepper motor increments is generated within the software.

3.6. Final Checks

Once the optical system is properly aligned and focused, the flash lamp coupling is optimized. It has been observed that the fiber optic coupling to the flash lamp can affect the signal-to-noise (SNR) of the instrument. This can be explained by non-uniformity in the arc generated across the electrodes of the flash lamp. By observing the noise structure of the recorded signal, while adjusting the coupling of the fiber optic cable to the flash lamp, it is possible to find the position of highest SNR. It is

important to note that the position equating to highest intensity, may not necessarily be the position of highest SNR. Additionally, the DC supply voltage to the flash lamps has been observed to influence the noise of the lamps. A galvanically isolated power supply should be used. Preliminary testing of a flash noise correction scheme, using a secondary spectrometer, was shown to be promising [2]. However, this relied on precise coupling of the two spectrometers, and is difficult to achieve in the current design iteration. Furthermore, recent release of a 20 W L12745 Xenon flash lamp from Hamamatsu provides significantly reduced signal noise, overcoming much of the benefit of secondary spectrometer correction.

Test scans of the system prior to experimentation with valuable samples are beneficial to assuring optimum data quality. A sharp meniscus and steep counterbalance edges in test scans are indicative of good alignment and focus. If time allows, the most revealing test of data quality is to perform an experiment on a well-characterized sample such as BSA. Evaluation with the 2DSA method in UltraScan3 across the relevant spectral range to be acquired is a particularly sensitive indicator of data quality [15]. The evaluation BSA results should yield S-Spectra of sharp monomer, dimer, and trimer peaks, across the UV spectral domain. For example see Pearson et al. [2].

4. Experimental Design and Data Acquisition

In the following pages we describe the essential principles of the AUC method, and how sample and data analysis considerations influence experimental design. This discussion is not meant to be a comprehensive account of all aspects of AUC, but is intended to provide an overview of the fundamentals and outline some of the most common types of AUC experiments. The basic principles of the AUC method, in regards to data acquisition settings and experimental design, will be given within the context of common analysis examples.

An AUC experiment records the redistribution of solutes in response to an applied centrifugal field. The experimental data may be acquired dynamically, known as sedimentation velocity, or at equilibrium. The following discussion will focus on the former, as velocity experiments are the most common type of modern AUC method used. Many excellent articles and book chapters have been written describing the theoretical principles of AUC experimentation [16–21]. The newcomer to AUC will also find a wealth of introductory material freely available through the Internet. The Internet resources are especially useful for learning to use the analysis software packages [22–25]. Many beginners find attending workshops invaluable to making effective use of the AUC method. This work offers guidance to the user of Open MWL-AUC technology for experimental design and optimizing data quality [11]. The general principles will apply to users of other absorbance optic AUC instrumentation, but the available acquisition settings may differ.

Sedimentation and diffusion coefficients (s and D) are the principle parameters that are recovered from AUC data, and may be modeled as a function of three solute properties: size, shape, and density. If one of the three is known, or may be assumed, then hydrodynamic models may be applied to estimate the other two. Two general approaches are considered for evaluating experimental data—simplified model interpretations that ignore or minimize diffusion—and finite element fitting techniques that model sedimentation and diffusion fluxes according to the Lamm equation [16,17,26]. Simplified model evaluation methods are typically used for generating an overview of solute distributions present in a sample, or for larger and heavier particles that sediment very quickly and cause very little diffusion flux during the time period of the experiment.

In order to achieve optimal data quality from AUC experiments, it is important to consider the appropriate experimental conditions for the sample under investigation. Many different variations of experimental techniques have been, and are continuing to be developed for AUC [27]. However, we will limit this discussion to focusing on three common sample types measured in this laboratory, and which are most instructive for understanding the principles of optimizing data acquisition: very small particles, very heavy particles, and 'mid-sized' particles.

All experimental techniques rely on precise thermal control of the rotor chamber, and most experiments are performed at ambient conditions. However, the centrifuge chamber may be cooled or heated to accommodate specific thermodynamic investigations or to mitigate sample instabilities. Operating at temperatures above 30 °C is not recommended, as significant amounts of oil vapor are released from the vacuum chamber and dirty the optics. Whatever temperature is selected, it is important that the rotor and samples are allowed to equilibrate before beginning the experiment.

Selecting a rotor speed requires careful consideration of the sedimentation characteristics of the sample, and what information content is required from the results. Larger, heavier particles will tend to sediment quickly and therefore require a slower rotor speed, while smaller, lighter particles will need a much greater centrifugal field to overcome diffusion. To aid in rotor speed selection, sedimentation rates may be estimated using reasonable assumptions about the sample properties and the classic Svedberg equation. Alternatively, AUC Lamm equation fitting programs may be used to simulate the sedimentation boundaries during an experiment [22,23,25].

Modern AUC rotors are limited to 60 krpm rotational speed, setting an upper limit on centrifugal fields. At lower rotor speeds the period of rotation is greatly extended, requiring much more time between radial data points and therefore longer to record a complete scan of the sample cell. For this reason, 3 krpm is typically a practical lower limit; however, some researchers have reported experiments as low as 1100 rpm. Scan time stamps in AUC data files are recorded as single values for each scan. However, depending on acquisition settings, a radial scan typically takes at least one minute to complete. Therefore, radial scan points near the bottom may be significantly distorted from the true temporal assignment. As a result, the scan time limit is one of the basic constraints for consideration when setting up an experiment. Low RPM experiment scan times will be rotor speed limited, while high RPM scan times will be limited by the flash lamp repetition rate or the readout rate of the spectrometer. Typical scanning parameters and the resulting scan times have been discussed previously [2,10]. Two easily modulated parameters by which MWL-AUC performance may be improved are through signal accumulation and averaging. The details of operation and the resulting signal to noise ratio benefit have been described recently [2]. In summary, signal averaging will serve to increase the SNR in general, while signal accumulation can improve the SNR of spectral regions with low emission or detection sensitivity. The number of acquisitions at each radial point will be a multiple of both parameter settings. The researchers must decide what degree of temporal scanning distortion is acceptable, and optimize the resulting trade-off with signal accumulation and averaging to improve SNR. The nature of the analytes and the purpose of the experiment are necessary to inform a decision.

As a first example, we may consider very heavy analytes, such as gold nanoparticle dispersions, where typical sedimentation coefficients range from hundreds to thousands of Svedbergs [5,28]. At a low rotor speed of 3 krpm, these types of particles will typically sediment the complete length of the cell channel between tens of minutes to a few hours depending on size. The number of radial point acquisitions, i.e., the multiple of averaging and accumulations, is typically set between 3 and 5, in order to limit scan times to between 1 and 2 min. It is important to recognize the diffusion information contained in AUC scans for very large particles is insignificant. For this reason, model free data transformations, e.g., g(s) or fitting methods that ignore diffusion are appropriate. Furthermore, large analytes such as gold nanoparticle dispersions are inherently polydisperse due to synthesis mechanisms. Therefore, the boundary spreading appearing in experimental data primarily arises due to sample polydispersity and instrument noise, and diffusion contributions are safely ignored. The aim of an AUC experiment with these types of analytes is most often to characterize subpopulations of solutes, or to approximate particle sizing through interpretations of sedimentation coefficients and other material properties. For samples of varying size and high polydispersity, AUC speed ramp methods can be especially useful [28].

Biomolecular investigations are some of the predominant motivations employing AUC technology. Proteins and protein complexes are particularly well suited to the size regime accessible by AUC.

Experiments typically range in length from 2 to 7 h for complete sedimentation, exhibiting the effects of diffusion through boundary broadening. The very low polydispersity, well-defined molecular weights, and good density estimation of proteins, allow precise extraction of additional molecular properties such oligomeric states, trace aggregates, or modeling interactions. Many types of nanoparticles, such as core–shell semiconductors, will sediment within a similar size regime, but will include a higher degree of polydispersity [7]. The choice of rotor speed must be carefully considered and can impose a large influence on the quality of the analysis. Model-independent analysis methods are often used as a first approximation to gain insight into the solute populations present and find reasonable estimates for upper limits of sedimentation coefficients. To further discriminate the solutes and improve sedimentation coefficient estimates, finite element modeling with Lamm equation solutions to fit for s and D information is typically necessary. The Lamm equation models are often reparameterized in terms of s and frictional ratios or molecular weight, using prior knowledge of partial specific volumes and substitution for D terms [16].

In some research, the aim is to discriminate the primary solute from subpopulations, such as identification of aggregates. For such experiments, higher rotor speeds will achieve better separation of components, by maximizing the physical separation of sedimentation boundaries and minimizing the diffusion broadening that can take effect over the time period of the experiment. In such cases, the s information in the recorded data is dominant, and the fitting technique may be described as 'correcting' for D. Meaning the D information recovered is subordinate, and serves to improve the resolution in sedimentation coefficients, but may not necessarily be a reliable value for independent interpretation. In other investigations, the goal is to accurately identify the molecular weight or oligomeric state or, additionally, to model a reversible association interaction of the samples. In this case, the user needs to accurately estimate, as well as possible, the sedimentation and diffusion information. This can be accomplished using a rotor speed that optimizes a balance of the sedimentation information, e.g., movement of the solute boundary, and the diffusion information, e.g., broadening of the boundary, in the experiment. At too high a speed, the particles will sediment quickly but not diffuse very much. This means there is boundary motion that is easily identified allowing for highly accurate estimates of the sedimentation coefficients, but minimal boundary spreading, causing fitting of the diffusion information to be unreliable. Conversely, at too slow a rotor speed, diffusion will dominate and instead of a concentration boundary propagating down the cell, a shifting exponential pattern is observed. In this case fitting for s will be compromised.

To optimize the contributions from sedimentation and diffusion, one should choose a speed such that the entire sample sediments completely down the cell channel over approximately 4 to 8 h. This rule of thumb allows for good fitting of both s and D in practice. For this class of analytes, rotor speeds are typically set between 30 and 50 krpm and the number of radial point acquisitions between 15 to 20, while still limiting scan times to between 1 and 2 min. A recent publication explored the relationship of analyte hydrodynamics, AUC rotor speed and data fitting through modeling of simulation data, suggesting a path to optimal rotor speed settings that minimize uncertainty of both s and D parameters [29]. Alternatively, one may choose to run the experiment twice, once at high speed, where the sedimentation is maximized and the best resolution of species in solution is enabled, allowing for optimal determination of the sedimentation coefficient. A subsequent experiment at lower speed can then be used to estimate the diffusion information. Having determined the number of solutes and corresponding s-values, these can be fixed in the analysis, and the fitting floated for D. Other researchers have implemented multispeed methods, where the rotor speed is increased at intervals within the experiment [20,29]. These methods have the same goal of optimizing both s and D parameters, but aim to do so within a single experiment. It should be noted that these multispeed methods are generally distinct from other speed ramp or gravitational sweep methods that use a continually varying rotor speed [19,30].

Researchers wishing to probe reversible associating solutes should run a sample at several different concentrations. A concentration dependence of the sedimentation coefficient is indicative of

binding kinetics on the time scale of sedimentation. The analysis of reversibly associating systems in AUC is complex, and a large volume of research has been devoted to the subject [31,32].

For an experiment with very small analytes, where measured sedimentation coefficients are less than 2 S, the rotor speed will necessarily be set to 60 krpm. Even with maximum centrifugal fields, particles in this size regime never produce the classic sigmoidal sedimentation boundary of AUC experiments. Instead, a shifting exponential is observed over the course of many hours. Experiments of 10 to 20 h are often incurred, as the solutes shift to a final equilibrium gradient across the cell radius. Nevertheless, numerical evaluation techniques have been shown to provide good fits to experimental data for particles down to a few tenths of one S [6]. For analytes such as this, a discernable change in the experimentally acquired data is observed only after tens of minutes. Therefore, a sensible choice of acquisition parameters may be selected to take advantage of the slow hydrodynamics. Increasing radial point acquisitions to between 20 and 30, where scan times need approximately 10 min, can typically yield excellent SNR without significantly distorting distribution results.

It is important to keep in mind that scan rates will increase as approximately two times the number of cells included in the rotor. Therefore, the data quality due to temporal distortion will be greater for experiments of higher numbers of cells. In contrast, the Beckman Coulter XL-A AUC cells are scanned sequentially; therefore, increasing the number of cells reduces the number of scans that may be acquired for each cell within an experiment, but does not introduce greater temporal distortions than what is initially present. The effect of scan distortions due to time stamps has not been fully explored. The preceding discussion provides an overview of general factors that are necessary for consideration when deciding on appropriate instrument settings, and some heuristic guidelines for beginners. For the researcher interested in exploring possibilities for improving AUC hardware, the discussion provides a framework of the physical constraints confronted in that pursuit. A detailed discussion regarding the acquisition triggering and subsequent speed dependent scan averaging characteristics is included in Appendix C, for the advanced user.

5. Discussion and Conclusions

Advancements in open-source MWL-AUC technology have made it an increasingly useful method for the analysis of particles and (bio)polymers in solution. The complexity of the hardware has limited the implementation of the instruments to a few laboratories. The details of results that may be achieved with MWL-AUC have been described previously for a diverse array of sample types and investigative questions [5–7,14,28,30,33–36]. However, previous publications documenting the performance of MWL-AUC have provided only cursory descriptions of the requirements to build and operate a complete system. The preceding pages detail the steps necessary for implementing this technology in a new laboratory. Systematic guidance for the alignment and focusing of the optical system allows new users to reliably generate good quality data. The examples of several sample types, considerations for experiment design and relevant acquisition settings have until now not been described in detail. We believe that providing this thorough account of the practical aspects regarding implementation and use of open-source MWL-AUC technology will encourage researchers to adopt the method in their own laboratories, and will be a useful resource for newcomers to the field.

6. Disclaimer Statement

The information provided in this manuscript should be used at the reader's discretion. The authors make no guarantees, either expressed or implied, nor assume liability for any unintentional consequences from the use of the instruments described herein.

Author Contributions: J.P. executed the design, building and testing of the instrument, and is the lead author. H.C. supervised the project and guided J.P. through the research.

Funding: J.P. thanks the Center for Applied Photonics (CAP) for financial support. We also thank Deutsche Forschungsgemeinschaft (DFG) for support of this project within SFB1214 project B6.

Conflicts of Interest: The authors declare no conflicts of interest.

Appendix A

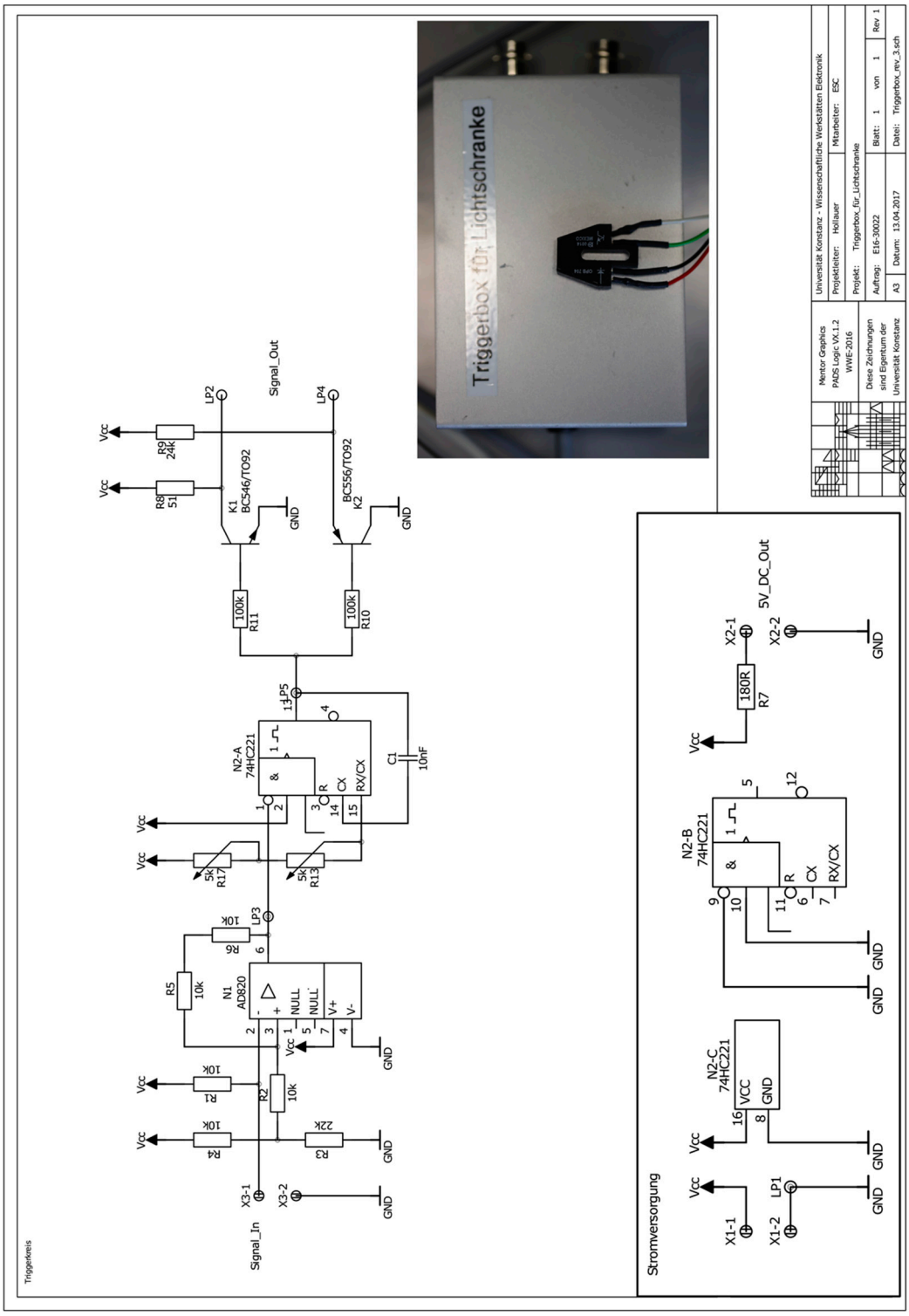

Figure A1. Electrical Schematic of reflective optical sensor and triggering electronics developed by the Universität Konstanz Electronics Workshop.

Appendix B. Step-by-Step Protocol for Alignment

Appendix B.1. Important Notes

- Xenon lamps emit strong UV radiation that is damaging the eye. Use proper eye protection when working with Xenon lamps.
- Take care when using laser diodes and do not point into eyes.
- The MWL-AUC is equipped with a turbomolecular vacuum pump. Do NOT open vacuum chamber (i.e., press 'Vacuum') before the turbo pump is below 400 Hz. Otherwise, damage to the pump may occur.
- Do NOT touch mirrors. UV coating will be destroyed. Clean by wetting a tissue with ethanol and gently dragging (without force) across mirror.

Refer to the Figures in the Main Text for Part Number References

Appendix B.2. Install Illumination Optics

- Sliding stage (Figure 3a #36) and vertical connector (Figure 2f #34) should be installed on the arm before installation.
- Install fiber tip slit adapter (Figure 4c #26) onto vacuum side end (in the chamber) of fiber optic cable. The fiber optic cable may have a core diameter of 100–400 um. The tip slit adapter then restricts the core diameter in the radial dimension (the dimension that is the primary determinant of resolution). The tip slit adapter is glued to the end of the SMA fiber connector (Figure 4a #27).

Appendix B.3. Illumination Collimation—Setting Fiber Tip to Focal Point of First OAPM

- Position SMA fiber connector exit tip (with tip slit adapter glued on) in OAPM collimator so light is collimated (Figure 5a #29). To find best collimation, shine the beam on to a distant surface (>30 cm), adjust SMA adapter barrel length while looking for best collimation. Make sure slit orientation is parallel to the bottom of the optical arm.
- Install focusing illumination OAPM (Figure 4a #31) in lower illumination assembly (Figure 4a #30). (Normally this can stay in place during disassembly/reassembly.)
- Install OAPM collimator (with fiber now attached) to lower illumination assembly of sliding arm, making sure fiber connection is rotated to align vertically (Figure 5a #28). Set in thermal can channel near approximate position.
- Install arm by carefully inserting over the lower illumination assembly. Note; the vertical connector bar (Figure 2f #34) must slide between the fiber optical cable and the lower illumination assembly.
- Attach lower illumination assembly to vertical connector bar with two pan head screws.

Note: make sure there is enough clearance between the illumination optics and rotor. Adjust height with two screws (Figure 2f #35) through slot in vertical connector bar if necessary (XLA is ~2.5 mm—should be greater than this).

- Position arm so that illumination mechanics are as close to the center of the rotor as possible (i.e., nearly touching the inner edge of the slot in the chamber can).

The first installation of the arm requires careful alignment by eye, such that the sliding mechanics of the arm move along a radial trajectory from the center of the rotor. The arm must also be set such that the sliding range will cover the distance from the top of the sample channel (towards the rotor center) to the bottom of the channel (towards the rotor edge). Use the sliding guide block (Figure 2e #19) to set the position and for reference when making minor adjustments.

- Make adjustments to level arm

Near the ends of each slotted detector arm base hole are 4 screws (Figure 2f #21) threaded through the base of the detector arm. The four screws may be tightened to adjust the level of the detector arm, while using a machinist balance on the top of the arm. This procedure must be done by simultaneously loosening/tightening the fastening screws and tightening/loosening the leveling screws.

Appendix B.4. Align Illumination Parallel and Coincident with the Optical Axis

- Attach lower imaging OAPM assembly (Figure 4d #37), without OAPM, to the sliding stage assembly (Figure 3a #36) on the arm.
- Install cross-bar device (Figure 2a #23) below lower imaging OAPM (Figure 4d #37), in the hole where the lower iris fits.
- Connect with optics tubes, to the cross-hair/screen assembly (Figure 5b #24).

Note: this assembly is mechanically centered along the focal point axis of the lower imaging OAPM, and is to be parallel and coincident with the desired illumination light path of the imaging optics.

- Attach laser diode (Figure 2d #22) to fiber input.
- Adjust illumination-focusing mirror (Figure 4a #31) by tilting with 4-corner 0.71 mm Allen wrench screws (Figure 4a #33) and/or sliding in channel.

The illumination beam should project the cross-bars shadow centered onto the cross-hairs, and the brightest center of beam cross section should also be coincident with cross-hairs. See Figure 6a in main text. Examples of how the alignment may be incorrect are shown in Figure 6b–d.

- Install illumination aperture assembly (Figure 4b #32) over illumination focusing OAPM (Figure 4a #31). Adjust aperture plates to limit stray light. Opening should be ~2.5 mm long and centered on beam.

Appendix B.5. Install Imaging Optics

- Disassemble and reinstall 1st Imaging OAPM assembly (Figure 4d #37) with mirrors (Figure 4d #48) and lower iris (Figure 5a #39). A 90° plane mirror (Figure 4d #38) is glued to the lower imaging assembly.
- Loosely install the 2nd OAPM assembly (Figure 7a #40) without the 2nd OAPM.
- Make sure that the 1st imaging OAPM beam is directed at the center attachment hole of the 2nd imaging OAPM assembly. To do this, close the iris below the 1st imaging OAPM (Figure 4d #39) to make the beam small; then make adjustments and view the beam with a piece of weight paper (Figure 5c #43), and mark position of 2nd OAPM assembly.
- Uninstall and reinstall 2nd OAPM assembly with OAPM (Figure 5a #42), also attach iris (Figure 5a #41) between mirrors. Align to marks and secure to sliding stage.

The OAPM is fastened to the assembly with a 3 mm steel ball between the center back of the mirror and a set-screw. Three screws thread into the back of the mirror, through the upper imaging assembly and may be used to adjust the trajectory of the beam off the 2^{nd} imaging OAPM (Figure 5a #44).

- Disconnect laser diode from fiber.
- Install camera (Figure 2c #25) at spectrometer position. Set the camera mounting plate to distance of OAPM focal length (101.6mm). Note: first install camera directly in-line with the other optics, then install the 2nd 90° plane mirror at a later step. Using CCD IR video camera and USB adapter; Software: Honest-tech TVR 2.5.
- Connect a low-power light source to the fiber input. For example, a flashlight set back from entrance of the fiber entrance connector. Too much light will saturate and blur the image on the CCD camera.

- Use 2nd imaging OAPM adjustment screws (Figure 5a #44) to direct light spot to the center of the camera. The trajectory of the beam projected off the mirror may be adjusted by simultaneously tightening/loosening the middle set-screw, and loosening/tightening the three attachment screws in the back of the mirror, or vice versa.
- Use the adjustment screw (Figure 5a #47) on the lower imaging assembly to raise and lower the 1st imaging OAPM and bring the spot on the CCD camera into focus on the computer screen (Figure 7b #46). It is useful to repeat this step, both with and without a cell in the rotor positioned in the beam path. This way the effects of the cell windows on focusing become apparent and may be compensated for.
- Remove spectrometer mounting plate.
- Reinstall spectrometer mounting plate and CCD camera in 90° position (Figure 3a #50).
- Install the 2nd 90° mirror (Figure 7a #49) between the 2nd imaging OAPM and the CCD camera. Find beam slit focused to approximate center of camera.
- Adjust the distance of the spectrometer mounting plate/CCD camera to bring slit spot into focus again. Note; the 1st imaging OAP should already be in the correct focus position from the previous steps.
- Check focus again through an empty cell positioned in the rotor within the beam path.
- Remove camera and install spectrometer.
- Connect fiber optic cable to Xenon flash lamp.
- Trigger lamp with NI-MAX application (details specific to Cölfen Laboratory).

->Devices and Interfaces -> NI PCI-6602 -> Testpanels
Set to Frequency = 10
View signal intensity with Spectrasuite. The integration time of the spectrometer should be set to match the frequency of the lamp pulses (10 Hz -> 100 ms).

- Use the 2nd imaging OAPM adjustment screws (Figure 5a #44) to direct light spot to hit spectrometer slit. This should be only a slight vertical shift. Watch intensity in Spectrasuite to find beam direction of maximum intensity.

Appendix B.6. Check Installation Positioning and Radial Alignment

*! Make sure everything is tight! If something comes loose and falls onto the spinning rotor the result would be catastrophic.

*! Check stepper motor limits! If stepper motor goes too far and hits the end of the track it could self-destruct and fall onto the spinning rotor.

- Use Zaber Console application to find limit position (Example details, specific to Cölfen laboratory)

Com 1 -> Open -> T-LA28A Actuator
Home—goes to 0
Move Absolute to find ~1 mm from end (Typically 180,000–210,000 steps)
Send home again

- Use conversion factor to calculate distance and set this in MWL–OS Application
- Check if the scanning track vector is aligned with radial vector of the rotor

    - First find the top and bottom of a cell: With the rotor spinning at 3000 rpm, run the angle calibration program and try taking scans at different stepper motor positions (first set the step angle to 1 degree, and scan a large angle range to find the cell). The bottom of the cell should be at least ~1 mm before the scanning limit (as determined before) of the motor.

- Write down the sample and reference sector center position angles near the channel bottom and do the same with the stepper motor set near the channel top. The angles should be less than 0.25 degrees different. If they are greater than 0.25 deg different; stop the AUC, rotate the detector arm by loosening the screws that attach it to the heat sink base plate, move the arm, retighten the screws, and test again.

Note: the slider guide block (Figure 2e #19) piece next to arm mounting plate is useful for making small adjustments. Can make a note of which way it is rotated, and if that makes the angle measurement difference better or worse. This will speed up the process of finding the aligned position. Note: tightening the screws attaching the arm to the baseplate can sometimes cause the arm position to move slightly. Slowly alternate tightening the screws on each side of the arm to achieve best alignment.

- Recheck that arm is leveled after each adjustment

Note; to prove that arm machined angles, etc. are correct, can check that arm leveling does indeed correspond to parallel with the vertical axis through the cell. For this a 1" cylinder was manufactured with a 0.5 mm hole through the center, by adjusting the level of the arm, can see that maximum light through the hole is achieved when arm is at true level.

Appendix B.7. Final Focusing and SNR Check

- Recheck best focus position of imaging optics.
- Set stepper motor to ~1/2 way extended, with rotor in chamber with 1 empty cell.
- Trigger light source, synchronized with Spectrasuite.

Integration time should correspond with lamp trigger (100 ms <-> 10 Hz).

- Adjust focusing screw (Figure 2g #47) of lower imaging OAPM to find highest intensity position; do this while alternating through a cell or through empty space.
- Find focus position where intensity maximum is approximately the highest both through the empty cell and the empty space.

This assures a position that will not be adversely effected by the refractive index of the solution. May require a small degree of simultaneous readjustment of z-x upper OAPM screw (Figure 5a #44) to hit center of the spectrometer.

- Leave iris open and adjust lamp output to good intensity. Find maximum intensity where the spectrum peaks are still below saturation.
- Close lower iris (Figure 5a #39) until intensity begins to drop.
- Close middle iris (Figure 5a #41) until a small drop in intensity is noticed, this will minimize stray light.
- Make sure fiber to lamp connection is at position of best SNR:

  - Custom Labview application is used to monitor SNR in real time and is available from the authors on request.
  - Adjust positioning while monitoring SNR.
  - Make sure there are no spikes at high repetition rate (>200 Hz).
  - Power supply voltage setting to the lamp has been observed to effect prevalence of flash spikes; adjustment may be necessary.

Appendix B.8. Software Calibrations

- Install the empty 2-channel cell in position 2 and counterbalance in position 4.
- Make angle calibration:

- Set stepper to approximate middle of cell channel
- Make angle calibration over rotor speed range
- Load, save and set as default the new angle calibration

- Make radial calibration:
  - Load the angle calibration made in the previous step.
  - Make radial calibration at 2000 rpm.
  - Set Motor range to cover top and bottom cell positions determined earlier.
  - Select the top and bottom edges of the counterbalance blades with vertical selectors. -> Calibrate positions: -> Home.
  - Load, save, and set as default the new radial calibration.
- Make test scans:
  - Check intensity.
  - Check that meniscus is sharp, that cell edges are sharp, and that counterbalance edges are where they should be.

Note: at low rotor speeds the meniscus will sag due to the earth's gravitational field, i.e., the meniscus shape will change at speeds up to ~15 krpm. Above 15 krpm the meniscus shape remains constant, therefore test scans should be taken at >15 krpm to assess meniscus shape.

Appendix C

At higher rotor speeds, the scan rate becomes limited by either the flash lamp repetition rate or the readout of rate of the spectrometer. Assuming some typical scan parameters we can consider the basic limits imposed. A sample channel is 12 mm in length, and a scan is typically discretized into 50 μm steps leading to 240 steps to scan one channel. Therefore, assuming a scan is allowed 1 min duration, each step is composed of 250 ms. When, also considering a typical 16 flash averaging setting of the Open MWL-AUC detector to achieve one minute scan time, and the fact that a cell is always scanned with two channels, the average time to acquire a spectra from each flash is 7.8 ms. The Ocean Optics spectrometers have a minimum integration time of 1 ms, and maximum trigger rate of 344 Hz. Because 344 Hz equates to a period of 2.91 ms, we can conclude the maximum readout rate is therefore 2.91 ms, leaving 4.89 ms between individual acquisitions, not including the time to move the stepper motor across radial steps. In practice the scan time is even better than this. A test scan of one cell using these settings (60 krpm, 16 averages, 14 mm channel, 50 μm steps) takes 50 s, resulting in an approximate 5.6 ms/acquisition rate. This leaves ~2.7 ms between acquisitions for software resetting, not including the time to move the stepper motor. A timing diagram in Figure A2 illustrates the operation for each acquisition of a typical 60 krpm scan. The acquisitions are then repeated for each of the 16 acquisitions to be averaged, for each channel of every cell, and for every step of the scan. Note that the spectrometer integration is triggered before the flash lamp is fired. This is inconsequential because the timing of the flash lamp is the critical parameter necessary for synchronization.

What becomes immediately evident is that the rotor passes the detector several times for each acquisition. This provides opportunity to make use of an alternative acquisition strategy. The software also provides the possibility to adjust the number of flash accumulations. In this mode, a number of successive flashes may be acquired onto the spectrometer chip, accumulating an integral amount of signal. To do this, the integration time of the spectrometer is set to match the timing duration required for a given number of flashes. The subsequent readout and processing time follows as before. A timing diagram illustrates the operation for each acquisition Figure A3 Subsequent acquisitions may be averaged further as in the previous description.

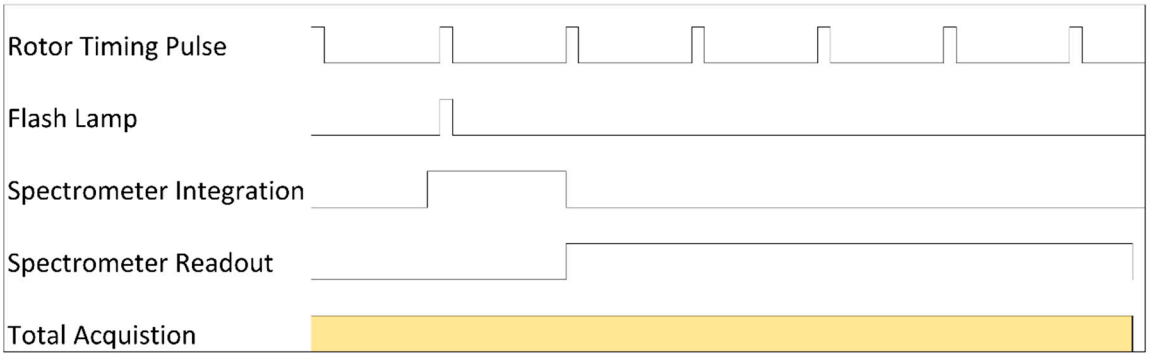

Figure A2. Synchronization timing diagram for a single acquisition in a typical MWL-AUC data collection setup. Note: not drawn to scale.

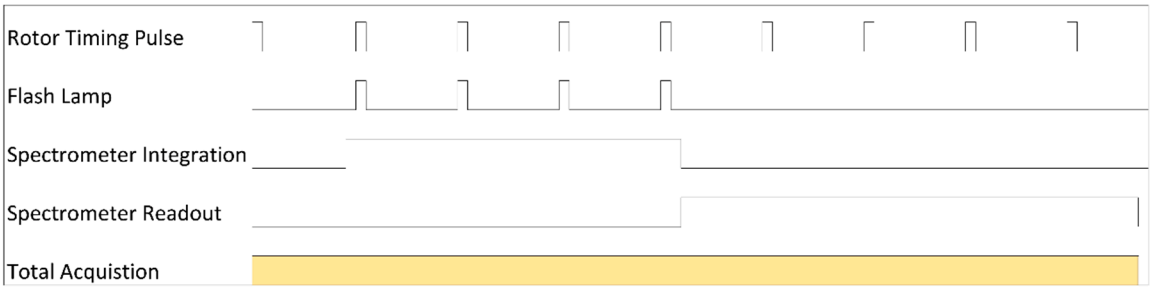

Figure A3. Synchronization timing diagram for 4 flash accumulation acquisition settings in a typical MWL-AUC data collection setup. Note: not drawn to scale.

This has several potential advantages. First, the original inspiration for this mode was to allow acquisitions from regions of the spectra that have low signal availability, such as the UV or near-infrared (NIR). Indeed, this acquisition mode works very well for that purpose by accumulating signals from multiple flashes. Additionally, we now have the opportunity to decrease the scan time by acquiring flashes from successive rotor passes. This works by lowering the illumination intensity, and then accumulating enough flashes to achieve a good signal level; generally 20,000–50,000 spectrometer counts. Because integrating flashes has the effect of averaging out flash-to-flash fluctuations, a similar SNR increase is observed as if a typical acquisition-averaging mode had been used, i.e., SNR increases as the square root of the number of acquisitions.

Furthermore, lowering the illumination intensity is most easily achieved by lowering the main discharge capacitor trimmer on the flash lamp. This also decreases the flash-to-flash variability and has the benefit of improving the life of the lamp. Moreover, the degradation of the fiber optic cables is observed to scale with lamp intensity, and thus the life of the cables will be extended.

Predicting the performance of this mode is complicated by the flash lamp noise dependency on repetition rate and also by the fact that certain rotor speed/flash accumulation combinations may provide an acquisition time that corresponds to slightly before a rotor pass, not allowing enough time to generate a signal for the next accumulation. The software must then delay to the subsequent rotor pass to begin the acquisition. These complications can be appreciated by observing data from some test scans through an empty rotor hole. Here, scans are taken with a rotor speed of 60 krpm, and two data sets are generated. The first uses a software setting for 16 single flash averages per data point. The second uses four averages, where each acquisition is accumulating four flashes; effectively collecting 16 flashes per data point. A scan was taken through empty space across a 2.5 mm scan segment, with 50 µm steps. The small scan segment minimizes any possible radial noise dependency. The SNR was then calculated from the average and standard deviation of the 50 resulting data points. A spectral signal was selected to compare matching intensities (600 nm for the first settings and 700 nm

for the second settings), where both provided ~35,000 counts. The repetition rate limit of the system is then modulated within the software settings from 1 to 5 ms (i.e., 1000 to 200 Hz). To compare the performance of the various settings, an effective SNR is calculated. First the SNR is divided by the square root of the number of flashes: SNR/Flash. The number of flashes is divided by the scan time to yield flashes/second. Multiplying the flash/second by 60 gives an estimate of the number of flashes that can be made in one minute using these settings. The effective SNR (SNR_{eff}) for a one-minute scan is then computed by rescaling based on the number of possible flashes in a one-minute scan time, Equation (A1):

$$SNR_{eff} = \left(\frac{\overline{X}}{\sigma}\right)\left(\frac{1}{\sqrt{N}}\right)\sqrt{\frac{N60}{t}} \quad \text{(A1)}$$

where $\overline{X}$ is the signal average, σ is the standard deviation, N is the number of flashes, and t is the scan time. Therefore, a scan that is longer than one minute will have an SNR_{eff} lower than that observed, and scans shorter than one minute will have an SNR_{eff} higher than observed. This approximates what would be achieved if one were to modulate the settings to each achieve a one-minute scan time. The performance can then be compared on a one-minute scan time basis. The SNR_{eff} is plotted against the repetition rate limitation setting, and corresponding scan times are included on the secondary axis, Figure A4.

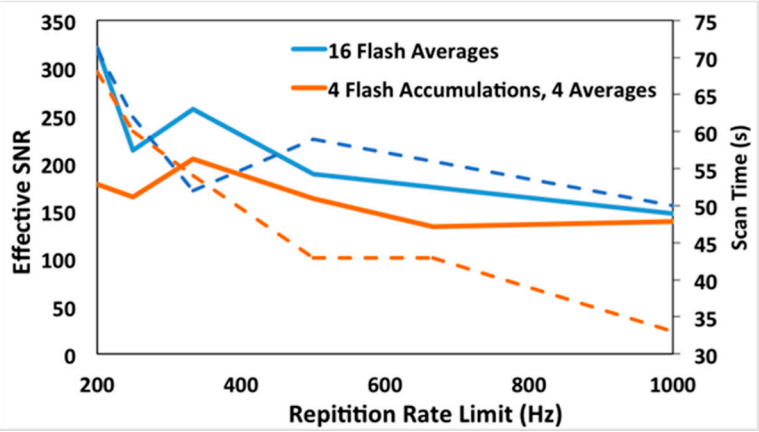

Figure A4. Plots of acquisition repetition rate versus effective signal-to-noise ratio (SNR_{eff}) for single flash accumulation with 16 averages for 4 flash accumulation and 4 averages settings (solid lines). Acquisition rates versus effective scan times plotted on the right axis (dotted lines).

In reality, only an integer number of flashes can be acquired. These observations will also be dependent on the signal intensity. For example, in the UV, where limited signal is available, single flash settings will achieve a much lower SNR, because a high count rate (>10,000 counts) is not possible with only one flash.

When accumulating flashes at lower rotor speeds, the integration time is increased within the software to accommodate the increased period of rotation, thus extending the scan time. If the rotor speed is selected that is lower than the corresponding flash repetition rate setting, then the scan rate will become rotor speed limited. For example, a rotor speed of 12,000 rpm is equivalent to 200 Hz, or a period of rotation of 5 ms. Therefore, if the repetition rate is set at or above 5 ms, the scan time will increase, or remain constant, for rotor speeds above 12,000 rpm, but will increase when lower rotor speeds are selected. It is useful to keep in mind that the rotor speed and revolution period follow an inverse relationship, Figure A5.

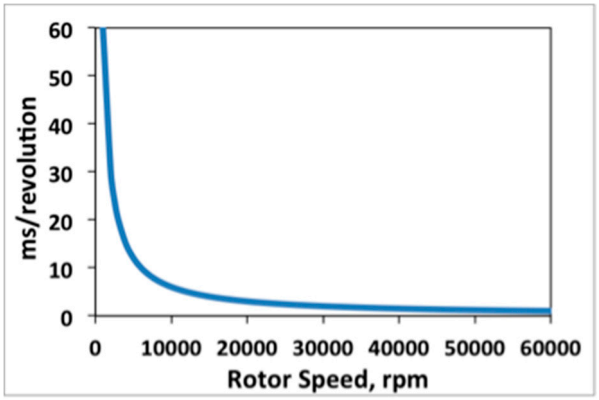

Figure A5. Inverse relationship of rotor speed versus period of rotation.

For comparison, a test scan at 3 krpm was made. A setting of four averages and no accumulations was used, with all other factors identical to the 60 krpm test scans. For these settings a single cell is scanned in 80 s. Following the same logic as before, results in a 35.7 ms/acquisition rate, and SNR_{eff} = 198. The relevant data in Figure A4 is included with relevant parameters, Table A1.

Table A1. Resulting acquisition repetition rate and SNR_{eff} for several flash accumulation and flash averaging settings.

krpm	Ave.	Accu.	T (s)	Hz	t (s)	$SNR_{obs.}$	SNR/flash	* Flash/s	'Flash'/min	$SNR_{eff.}$
60	16	1	0.005	200	71	349	87.25	0.225	13.52	321
60	16	1	0.004	250	62	217	54.25	0.258	15.48	213
60	16	1	0.003	333	52	239	59.75	0.308	18.46	257
60	16	1	0.002	500	59	187	46.75	0.271	16.27	189
60	16	1	0.001	1000	50	134	33.50	0.320	19.20	147
60	4	4	0.005	200	68	189	47.25	0.235	14.12	178
60	4	4	0.004	250	60	165	41.25	0.267	16.00	165
60	4	4	0.003	333	54	194	48.50	0.296	17.78	204
60	4	4	0.002	500	43	138	34.50	0.372	22.33	163
60	4	4	0.0015	667	43	113	28.25	0.372	22.33	133
60	4	4	0.001	1000	33	103	25.75	0.485	29.09	139
3	4	1	0.02	50	80	229	114.50	0.050	3.00	198

It is evident from the results that the possible benefits of applying the flash accumulation settings, is offset by the strong dependence of the flash rate on SNR. Lower flash rate settings, despite extending the scan time and limiting the number of averages, has a significant benefit on SNR. It is important to note, the data in Table A1 is presented only for the purpose of illustrating the relationship of SNR and various experimental parameters. For example, if a user wishes to measure multiple samples in a run, the scan time will increase approximately as two times the number of cells. When conducting a MWL AUC experiment, the user should consider aspects of the data acquisition specific to their research questions, as discussed in the main body of the paper, and design the experiment accordingly. This includes selection of the instrument settings in addition to an appropriate rotor speed.

References

1. Bhattacharyya, S.K.; Maciejewska, P.; Börger, L.; Stadler, M.; Gülsün, A.M.; Cicek, H.B.; Cölfen, H. Development of a fast fiber based UV-Vis multiwavelength detector for an ultracentrifuge. In *Analytical Ultracentrifugation, Progress in Polymer and Colloid Science*; Springer: Berlin/Heidelberg, Germany, 2006; Volume VIII, pp. 9–22.

2. Pearson, J.; Walter, J.; Peukert, W.; Cölfen, H. Advanced Multiwavelength Detection in Analytical Ultracentrifugation. *Anal. Chem.* **2017**, *90*, 1280–1291. [CrossRef] [PubMed]
3. Strauss, H.M.; Karabudak, E.; Bhattacharyya, S.; Kretzschmar, A.; Wohlleben, W.; Cölfen, H. Performance of a fast fiber based UV/Vis multiwavelength detector for the analytical ultracentrifuge. *Colloid Polym. Sci.* **2008**, *286*, 121–128. [CrossRef]
4. Karabudak, E.; Cölfen, H. The Multiwavelength UV/Vis Detector: New Possibilities with an Added Spectral Dimension. In *Analytical Ultracentrifugation: Instrumentation, Software and Applications*; Springer: Berlin, Germany, 2016; pp. 63–80.
5. Pearson, J.; Cölfen, H. LED based near infrared spectral acquisition for multiwavelength analytical ultracentrifugation: A case study with gold nanoparticles. *Anal. Chim. Acta* **2018**, *1043*, 72–80. [CrossRef] [PubMed]
6. Pearson, J.; Nguyen, T.L.; Cölfen, H.; Mulvaney, P. Sedimentation of C60 and C70–Testing the Limits of Stokes' Law. *J. Phys. Chem. Lett.* **2018**, *9*, 6345–6349. [CrossRef] [PubMed]
7. Walter, J.; Gorbet, G.; Akdas, T.; Segets, D.; Demeler, B.; Peukert, W. 2D analysis of polydisperse core–shell nanoparticles using analytical ultracentrifugation. *Analyst* **2017**, *142*, 206–217. [CrossRef]
8. Zhang, J.; Pearson, J.Z.; Gorbet, G.E.; Cölfen, H.; Germann, M.W.; Brinton, M.A.; Demeler, B. Spectral and Hydrodynamic Analysis of West Nile Virus RNA–Protein Interactions by Multiwavelength Sedimentation Velocity in the Analytical Ultracentrifuge. *Anal. Chem.* **2016**, *89*, 862–870. [CrossRef]
9. Pearson, J.; Hofstetter, M.; Dekorsy, T.; Totzeck, M.; Cölfen, H. Design concepts in absorbance optical systems for analytical ultracentrifugation. *Analyst* **2018**, *143*, 3961–4208. [CrossRef]
10. Pearson, J.; Krause, F.; Haffke, D.; Demeler, D.; Schilling, K.; Cölfen, H. Next Generation AUC adds a Spectral Dimension: Development of Multiwavelength Detectors for the Analytical Ultracentrifuge. In *Methods in Enzymology*; Cole, J.L., Ed.; Burlington Academic Press: Burlington, MA, USA, 2015; Volume 564.
11. Cölfen, H.; Laue, T.M.; Wohlleben, W.; Schilling, K.; Karabudak, E.; Langhorst, B.W.; Brookes, E.; Dubbs, B.; Zollars, D.; Rocco, M.; et al. The Open AUC Project. *Eur. Biophys. J. Biophys.* **2010**, *39*, 347–359. [CrossRef]
12. Walter, J.; Peukert, W. FAU Erlangen AUC Research. Available online: http://lfg.fau.de/research/AUC/ (accessed on 1 February 2019).
13. Walter, J.; Segets, D.; Peukert, W. Extension of the Deep UV-Capabilities in Multiwavelength Spectrometry in Analytical Ultracentrifugation: The Role of Oil Deposits. *Part. Part. Syst. Charact.* **2016**, *33*, 184–189. [CrossRef]
14. Walter, J.; Lohr, K.; Karabudak, E.; Reis, W.; Mikhael, J.; Peukert, W.; Wohlleben, W.; Colfen, H. Multidimensional Analysis of Nanoparticles with Highly Disperse Properties Using Multiwavelength Analytical Ultracentrifugation. *ACS Nano* **2014**, *8*, 8871–8886. [CrossRef] [PubMed]
15. Brookes, E.; Cao, W.M.; Demeler, B. A two-dimensional spectrum analysis for sedimentation velocity experiments of mixtures with heterogeneity in molecular weight and shape. *Eur. Biophys. J. Biophys.* **2010**, *39*, 405–414. [CrossRef] [PubMed]
16. Cole, J.L.; Lary, J.W.; Moody, T.P.; Laue, T.M. Analytical ultracentrifugation: Sedimentation velocity and sedimentation equilibrium. *Method Cell Biol.* **2008**, *84*, 143–179. [CrossRef]
17. Correia, J.J.; Stafford, W.F. Sedimentation velocity: A classical perspective. In *Methods in Enzymology*; Academic Press: Cambridge, MA, USA, 2015; Volume 562, pp. 49–80.
18. Demeler, B.; Gorbet, G. Analytical Ultracentrifugation Data Analysis with UltraScan-III. In *Analytical Ultracentrifugation: Instrumentation, Software, and Applications*; Uchiyama, S., Arisaka, F., Stafford, W.F., Laue, T., Eds.; Springer: Tokyo, Japan, 2015.
19. Mächtle, W.; Börger, L. *Analytical Ultracentrifugation of Polymers and Nanoparticles*; Springer Science & Business Media: Berlin, Germany, 2006.
20. Schuck, P.; Zhao, H.; Brautigam, C.A.; Ghirlando, R. *Basic Principles of Analytical Ultracentrifugation*; CRC Press: Boca Raton, FL, USA, 2016.
21. Scott, D.J.; Harding, S.E.; Rowe, A.J.; Royal Society of Chemistry (Great Britain). *Analytical Ultracentrifugation: Tehniques and Mehods*; RSC Pub.: Cambridge, UK, 2005; p. xxiii. 587p.
22. Demeler, B.; Gorbet, G.; Zollars, D.; Dubbs, B. UltraScan-III Version 3.3: A Comprehensive Data Analysis Software Package for Analytical Ultracentrifugation Experiments. Available online: http://www.utrascan3.uthscsa.edu/ (accessed on 1 April 2015).
23. Schuck, P. SEDFIT. Available online: http://www.analyticalultracentrifugation.com/default.htm (accessed on 1 March 2018).

24. Philo, J. DCDT+. Available online: http://www.jphilo.mailway.com/dcdt+.htm (accessed on 1 March 2018).
25. Stafford, W. RASMB. Available online: http://www.rasmb.org/ (accessed on 1 March 2018).
26. Schuck, P.; Demeler, B. Direct sedimentation analysis of interference optical data in analytical ultracentrifugation. *Biophys. J.* **1999**, *76*, 2288–2296. [CrossRef]
27. Schneider, C.M.; Haffke, D.; Cölfen, H. Band Sedimentation Experiment in Analytical Ultracentrifugation Revisited. *Anal. Chem.* **2018**, *90*, 10659–10663. [CrossRef] [PubMed]
28. Walter, J.; Peukert, W. Dynamic range multiwavelength particle characterization using analytical ultracentrifugation. *Nanoscale* **2016**, *8*, 7484–7495. [CrossRef] [PubMed]
29. Gorbet, G.E.; Mohapatra, S.; Demeler, B. Multi-speed sedimentation velocity implementation in UltraScan-III. *Eur. Biophys. J.* **2018**, *47*, 825–835. [CrossRef] [PubMed]
30. Walter, J.; Sherwood, P.; Lin, W.; Segets, D.; Stafford, W.; Peukert, W. Simultaneous analysis of hydrodynamic and optical properties using analytical ultracentrifugation equipped with multiwavelength detection. *Anal. Chem.* **2015**, *87*, 3396–3403. [CrossRef]
31. Demeler, B.; Brookes, E.; Wang, R.; Schirf, V.; Kim, C.A. Characterization of Reversible Associations by Sedimentation Velocity with UltraScan. *Macromol. Biosci.* **2010**, *10*, 775–782. [CrossRef]
32. Schuck, P.; Zhao, H. *Sedimentation Velocity Analytical Ultracentrifugation: Interacting Systems*; CRC Press: Boca Raton, FL, USA, 2017.
33. Karabudak, E.; Backes, C.; Hauke, F.; Schmidt, C.D.; Colfen, H.; Hirsch, A.; Wohlleben, W. A Universal Ultracentrifuge Spectrometer Visualizes CNT-Intercalant-Surfactant Complexes. *ChemPhysChem* **2010**, *11*, 3224–3227. [CrossRef] [PubMed]
34. Karabudak, E.; Wohlleben, W.; Colfen, H. Investigation of beta-carotene-gelatin composite particles with a multiwavelength UV/vis detector for the analytical ultracentrifuge. *Eur. Biophys. J. Biophys.* **2010**, *39*, 397–403. [CrossRef]
35. Thajudeen, T.; Walter, J.; Srikantharajah, R.; Lübbert, C.; Peukert, W. Determination of the length and diameter of nanorods by a combination of analytical ultracentrifugation and scanning mobility particle sizer. *Nanoscale Horiz.* **2017**, *2*, 253–260. [CrossRef]
36. Wawra, S.E.; Pflug, L.; Thajudeen, T.; Kryschi, C.; Stingl, M.; Peukert, W. Determination of the two-dimensional distributions of gold nanorods by multiwavelength analytical ultracentrifugation. *Nat. Commun.* **2018**, *9*, 4898. [CrossRef] [PubMed]